

tion.

In studies related to meteorology based on such memory-based approach, T. Mohri *et al.* proposed a system to predict future weather categories (rain or fine) based on past similar situations; they used a weather database holding a large amount of symbolized weather data such as rain amount and wind direction measured at surface observatories (Mohri, Nakamura, & Tanaka 1993). E. K. Jones and A. Roydhouse developed a retrieval system for summarized weather maps that held low and high pressure data. The data was indexed with regard to position, extent, and central intensity of the phenomena (Jones & Roydhouse 1995). These studies dealt with high-level features or symbolized data of large-scale (1000km^2 - 10000km^2) phenomena whose changes were relatively smooth and slow. In contrast to the above methods, we directly employ raw image sequences and concentrate on smaller scale (10km^2 - 300km^2) and more dynamic phenomena that are full of abrupt changes.

Moreover, in the field of nonlinear dynamical systems, the idea of using similar past patterns has also been applied to predict chaotic time series such as market activity (Mulhern & Caprara 1994), and several prediction methods have been proposed (Ikeguchi & Aihara 1995). However, the targets of these existing schemes were mostly limited to one dimensional time series, and the attempt to handle image pattern has been hampered by the lack of a suitable method of representing complex, time-varying, two dimensional patterns.

In recent years, appearance-based methods have been developed for object and face recognition. In these methods, the high dimensional features of raw image intensity are transformed into a lower dimensional space, the so called eigenspace, based on principal component analysis of a set of training images (Murase & Nayar 1995) (Turk & Pentland 1991). Because of its robustness under real environments and its simplicity, explicit target modeling is not required, the range of applications continues to expand such as human gesture recognition (Bobick & Wilson 1995), robot vision system (Nayar, Nene, & Murase 1996), and video retrieval (Fujimoto *et al.* 1996).

In this paper, since we do not presuppose the availability of meteorological knowledge regarding physical precipitation phenomena, a sort of appearance-based representation is employed to handle complex echo patterns. In particular, this paper introduces the global distribution of echo patterns, the velocity field, and temporal texture features. While that first two features describe the global characteristics of the precipitation system, the temporal texture features characterize local non-rigid motion patterns, which are strongly related to the underlying structure of precipitation (Otsuka *et al.* 2000). These image features are transformed into the eigenspaces and the image sequence is represented as paths in the eigenspaces. The dissimilarity between two image sequences, used to retrieve similar past sequences, is defined as the normalized distance between the paths of feature points in eigenspaces of the image features. Forecast images are then constructed from a future point in the feature spaces, which is estimated by a nonlinear prediction scheme.

Although, similar representation schemes for time series of image features have been explored for motion recogni-

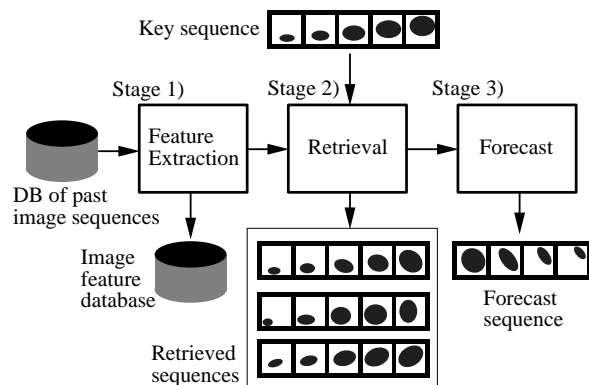


Figure 1: Framework of Memory-Based Forecasting of image sequence.

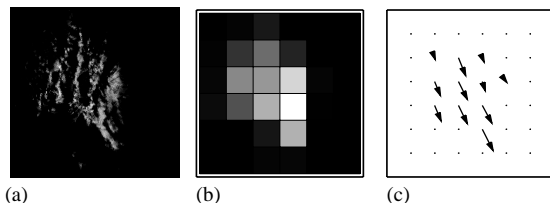


Figure 2: (a)Radar echo image, (b)Mesh feature, (c)Velocity field.

tion (Bobick & Wilson 1995) (Yacoub & Black 1999), current targets are mostly limited to artificially generated patterns, not naturally occurring patterns whose dynamics are unknown. Our research reveals the potential of the image sequence retrieval method in understanding natural systems and their veiled principles.

This paper is organized as follows. Section 2 introduces the framework and an implementation. Section 3 shows experimental results. Section 4 draws several discussions and a conclusion is presented in Section 5.

Framework and Implementation

The proposed MBF framework consists of three stages: feature extraction, retrieval, and forecast, as shown in Figure 1. At first, the sequence of image features representing the characteristics of the targeted image patterns are extracted from the image sequence database, which holds a large set of images. The image features are stored in the image feature database. Next, the latest image sequence (or arbitrary sequence) given as the query sequence is compared with each of the stored sequences in terms of feature vector difference to retrieve similar sequences. Finally, the subsequent sequences of the retrieved sequences are used to produce forecast information such as the accumulated distribution of precipitation in the case of weather forecasting.

Feature Extraction

The radar echo patterns present in weather radar images are non-rigid and deformable patterns that appear and disappear one after another, while roughly paralleling atmospheric flow. For example, Figure 2(a) shows a pattern, called the band-shape pattern, that consists of a set of small echo cells

forming parallel lines. Each echo cell continuously moves with atmospheric flow, while repeatedly appearing and disappearing. In spite of the constant movement of the echo cells, the whole pattern (pattern envelope) changes its shape and location slowly compared to cell movement. Such observations, note that the echo pattern varies its apparent motion characteristics according to the observation scale, correspond to the multiple scale structure of the precipitation system. Each scale has its own instinct property regarding spatial extents, speed, and lifetime of the echo pattern, but the phenomena on different scales are interrelated. In view of this scale dependent structure, the radar echo patterns are decomposed into two types of image features at different scales to characterize the precipitation system: global features and local features.

The global features represent the spatial distribution and movement of the entire echo pattern i.e. global position and shape of the pattern. Also, its changes through time represent the long-range motion such as translation, and growth and decay of the entire precipitation system. As the global features, the mesh feature $x_1(t)$ and the velocity field feature $x_2(t)$ are calculated for each time step t for the spatial distribution and motion of the echo patterns. As shown in Figure 2(b),(c), each image frame at each time step is partitioned into meshes, and the average gray level and average velocity of each mesh region are calculated as vector components of the mesh feature and the velocity field, respectively.

While the precipitation system roughly moves along with the atmospheric flow, the detailed characteristics of the precipitation phenomenon are reflected in the spatial and temporal structures of echo cells. Therefore, as local features, we focus on the statistical characteristics of an aggregation of echo cells, and introduce temporal texture features x_3 , which mainly measure the uniformity and diversity of the local echo motion(Otsuka *et al.* 1998). These temporal texture features are calculated based on an analysis of motion trajectories drawn by moving edges in local spatiotemporal space. They are able to characterize types of echo pattern such as band-shape, stratiform, and scattered-type, since the atmospheric structure of precipitation phenomenon can be segregated into specific types of texture and echo cell motion. A set of temporal texture features is calculated for each mesh as in Figure 2(b), and the average values of the feature values over the meshes at time step t become the feature vector $x_3(t)$.

For each set of the feature vectors, we compute eigenvectors and eigenvalues from their covariance matrices, and the feature vectors at each time step t are then correspondingly transformed into reduced vectors $y_1(t)$, $y_2(t)$, and $y_3(t)$ in eigenspaces to eliminate correlated components within a set of feature vectors and to reduce their dimensionalities. The eigenspaces are spanned by eigenvectors with large eigenvalues calculated from the covariance matrices of the feature vectors.

Representation of Echo Pattern Sequence

For the retrieval of similar pattern toward forecasting, it is required that not only query pattern (present pattern) and retrieved pattern at a time step are similar, but also their trend

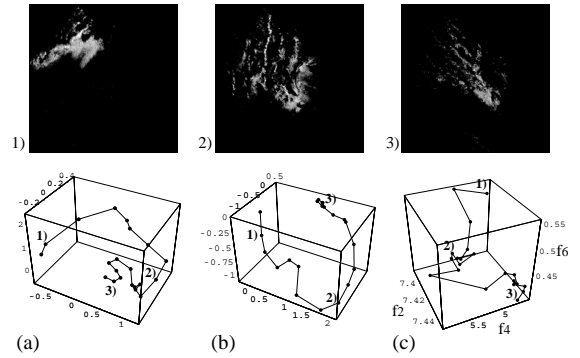


Figure 3: Paths of feature points of (a)Mesh feature in eigenspace, (b)Velocity field in eigenspace, and (c)Temporal texture [Axes : motion entropy f_2 , speed f_4 , density f_6]. Note, each point is 1 hour apart.

in pattern change should also be similar. To represent this trend, the pattern sequence is represented by a set of sequential feature vectors. Figure 3 shows paths of feature points for a sequence in the feature spaces. Matching the transition in the echo sequence, the feature points trace paths in the feature spaces representing the temporal development of the pattern. Therefore, the similarity between two sequences can be determined from the degree of closeness of their two paths.

Retrieval Process

Next, a retrieval algorithm based on path dissimilarity is presented. Hereafter the query sequence $\{T - L + 1, \dots, T - 1, T\}$ and the matching sequence $\{t - L + 1, \dots, t - 1, t\}$ are denoted by tail time T and t , respectively, where L is the length of the subsequences to be matched, as shown in Figure 4. This retrieval process consists of two steps: first, select retrieval candidates from the complete dataset; and second, rank the retrieved candidates by DP matching and to present candidates ranked in terms of closeness. Here, the distance measure between patterns at two time steps, m and n , in terms of feature k , is defined as

$$d_k(m, n) = \frac{\|\mathbf{y}_k(m) - \mathbf{y}_k(n)\|}{\eta V_k(T)} \quad (1)$$

where $\|\cdot\|$ represents Euclidean norm, and η is the lead time step that denotes the forecast target time. $V_k(T)$ indicates the transition speed of the query pattern corresponding to the distance that a feature point moves per unit time step in the feature space. For example, the transition speed $V_k(T)$ can be obtained as follows

$$V_k(T) = \|\mathbf{y}_k(T) - \mathbf{y}_k(T - 1)\|. \quad (2)$$

With the transition speed $V_k(T)$ and lead time η , we can calculate normalized distances $d_k(m, n)$. The numerator in Eq.(1) depends on types of the echo patterns, especially its area for the mesh feature. This normalization eliminates this dependency and enables us to set an appropriate search range by thresholding the distance $d_k(m, n)$.

Next, from the complete dataset, we extract subset S_T that holds retrieval candidate subsequences similar to the query

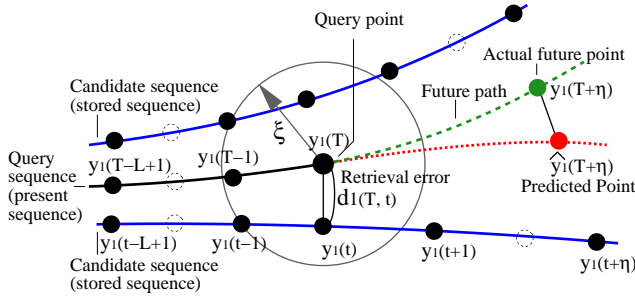


Figure 4: Paths representing query sequence and stored sequences in the feature space.

sequence T by thresholding the distance d_k calculated between the query point and each point in the dataset over the span L , as written in

$$S_T = \bigcap_{\substack{k \in \{1,2,3\} \\ i \in \{0, \dots, L-1\}}} \{t | d_k(T-i, t-i) < \xi\} \quad (3)$$

where ξ is a threshold determining the range of dissimilarity. The subset S_T consists of subsequences that display the similar phenomenon as the query.

Next, the dissimilarity between the query and each of the candidate sequences in S_T is determined to choose several of the best matching sequences. It is known that similar phenomena can exhibit different development speeds, and it is desirable to determine the degree of dissimilarity while compensating a certain degree of difference in their speeds. To do this, possible temporal alignments between query and the candidate sequence should be considered to select the one with minimum matching cost. Thus, we employ DP matching in determining the degree of dissimilarity $D_k(T, t)$ for each feature k . $D_k(T, t)$ is defined as described in the following recursive procedure.

$$D_k(T, t) = \min \left\{ \begin{array}{l} D_k(T-1, t) + d_k(T, t)/L \\ D_k(T-1, t-1) + d_k(T, t)/L \\ D_k(T, t-1) + d_k(T, t)/L \end{array} \right\}$$

$$D_k(m, n) = d_k(m, n)/L$$

if $m = T - L + 1$ or $n = t - L + 1$.

(4)

The total dissimilarity measure $E(T, t)$ between the query subsequence T and a subsequence t in the database is then obtained by integrating each retrieval error $D_k(T, t)$ as follows

$$E(T, t) = \frac{1}{R} \sum_{k=1}^R D_k(T, t) \quad (5)$$

where number of features $R = 3$. The total dissimilarity $E(T, t)$ is also called the retrieval error.

Finally, we select some retrieval sequences from the set of the retrieval candidates S_T , in ascending order of the total dissimilarity measure E . Here, we assume that the user gives the maximum number K of retrieved sequences and

the allowable total dissimilarity E_{TH} . The set of resulting retrieved sequences C_T is retrieved as

$$C_T = \{q_1, q_2, \dots, q_{K'}\} \quad (6)$$

where

$$E(T, q_i) \leq E(T, q_{i+1})$$

$$K' = \max\{i | i \leq K, E(T, q_i) \leq E_{TH}\}$$

$$|q_i - q_{i+1}| > r$$

$$q_1 = \arg \min_{t \in S_T} E(T, t)$$

where r is constant and used to prevent retrieving adjacent points. In Eq.(6), K' denotes the resulting number of the retrieved sequences.

Prediction Scheme

Finally, we generate the forecast image of the radar echo pattern at η time steps ahead, based on subsequent parts of the retrieved sequences C_T . To that end, we first predict the future point of the query sequence in the mesh feature space. Here, since we consider this as a nonlinear prediction problem of time series, we employed the modified Lorenz method (Ikeguchi & Aihara 1995) because of its stability. This method produces the prediction as the linear combination of points at η steps ahead of the retrieved points q_i in the feature space, and we define its coefficients as the inverse of the retrieval error of each retrieved sequence. The prediction point $\hat{\mathbf{y}}_1(T + \eta)$ in the mesh feature space is obtained as

$$\hat{\mathbf{y}}_1(T + \eta) = \sum_{i=1}^{K'} w(q_i) \mathbf{y}_1(q_i + \eta) \quad (7)$$

$$w(q_i) = \frac{1}{E(T, q_i)} \cdot \frac{1}{\sum_{j=1}^{K'} (1/E(T, q_j))}. \quad (8)$$

Next, we construct the forecast image $\hat{I}(T + \eta)$ from the predicted point $\hat{\mathbf{y}}_1(T + \eta)$. Since the transformation G that yields the mesh feature $\mathbf{y}_1(t)$ from the original image $I(t)$ is not one-to-one correspondence mapping, we can not unequivocally obtain the forecast image from the predicted point $\hat{\mathbf{y}}_1(T + \eta)$. Thus, we pose the constraint as described in $|\hat{\mathbf{y}}_1(T + \eta) - G(\hat{I}(T + \eta))| = 0$, and we obtain the forecast image that satisfies this constraint. Due to the linearity of the transformation G , which consists of spatial averaging and linear mapping into the eigenspace, the forecast image can be produced as

$$\hat{I}(T + \eta) = \sum_{i=1}^{K'} w(q_i) I(q_i + \eta) \quad (9)$$

from Eq.(7) and the above constraint.

Experiments

To confirm the effectiveness of the proposed method, we conducted statistical experiments on retrieval and prediction.

Preparation of Dataset

In advance of the experiments, the feature spaces were constructed using approximately 9000 hours of radar images

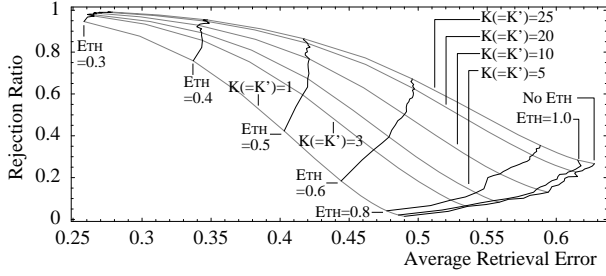


Figure 5: Relationship between average retrieval error and rejection ratio for various retrieval rank $K(=K')$ and threshold E_{TH} values.

(about 108000 image frames, 6 winter seasons) for the Sapporo area, northern Japan. Image size was 340×340 pixels where one pixel corresponded to a 1 km^2 area, and the gray level was 256 levels, which indicated instantaneous precipitation intensity. A single image frame was captured every 5 minutes. We set the unit time step to 1 hour, which meant that the interval between two adjacent time steps corresponded to 12 image frames. Dimensions of the eigenspaces were 8, 30, and 4 for the mesh feature, the velocity field, and the temporal texture feature, respectively. These dimensionalities were chosen to achieve 90% cumulative proportion, which means that 90% of the total variance in original feature distribution can be represented in the transformed feature space. The mesh size was 6×6 and each mesh included 55×55 pixels; the number of frames for temporal averaging was set to 20 frames. Subsequence length for matching was $L=3$, and the forecast lead time was set at $\eta=3$, the current goal of short-term precipitation forecasting. The threshold ξ was set to 1.0, and $r=3$. These parameters were empirically determined. Before each retrieval, the sequence used as the query, and its following sequence (if any), was removed from the dataset.

As a statistical evaluation of retrieval performance and prediction accuracy, we randomly picked 800 time steps as queries from a database holding about 9000 time steps. Each time step within the dataset was given as a query, and several sequences were retrieved to create the forecast image. After that, statistical characteristics regarding retrieval and prediction accuracy were examined. Here, the evaluation was done in the manner of the leave-one-out scheme.

Retrieval Error and Rejection Ratio

Figure 5 shows the relationships between the average retrieval error and the rejection ratio for various retrieval rank $K(=K')$ and threshold E_{TH} values. The rejection ratio was defined as the ratio of trials in which retrieval failed due to a lack of neighboring sequences. The retrieval result for retrieval rank $K(=K')$ corresponds to the result whose number of retrieved sequences K' is equal to the designated number of sequences K . From Figure 5, we can see that the retrieval error increases with retrieval rank $K(=K')$, and that a tradeoff between the retrieval error and the rejection

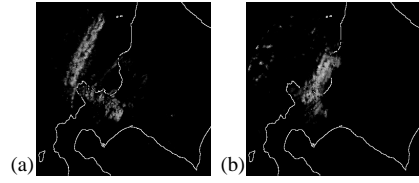


Figure 6: Query sequence, (a)Start frame, (b)End frame.

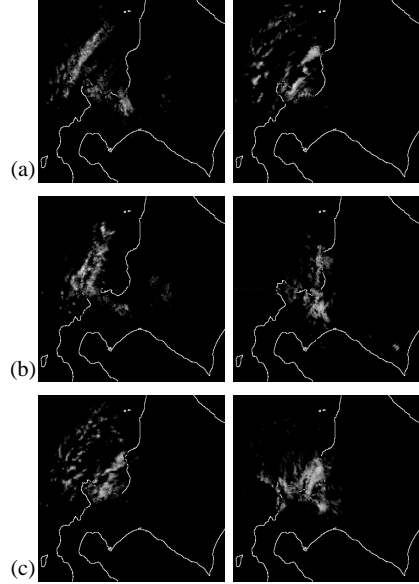


Figure 7: Retrieved sequences, (a)1st., (b)2nd., (c)3rd. candidate, [(left)start frame, (right)end frame].

ratio exists; small threshold E_{TH} offers retrieval with small retrieval error, but the rejection ratio tends to increase. Therefore, Figure 5 can be taken as a guide regarding data availability, an important factor in actual operational use.

As an example of retrieval, Figure 6 and Figure 7 show a query sequence and the top three retrieved sequences, respectively. Figure 6 includes a thick line-shaped echo moving toward the land area, and we can see that the retrieved sequences in Figure 7 also include patterns similar to the query pattern. These retrieval results are satisfactory because the retrieved patterns are not only visually similar to the queries, but also have almost the same meteorological characteristics as the query. Such retrieval results are expected to be useful reference information for human forecasters in understanding and forecasting future weather pattern.

Prediction Accuracy in Feature Space

Next, the prediction accuracy in the mesh feature space was verified. The reason for choosing the mesh feature was that the mesh feature was a kind of summarized representation of the precipitation distribution.

For each trial, the future point of the query sequence was predicted by using Eq.(7), and the prediction error ϵ_T was calculated as written in

$$\epsilon_T = \frac{|\hat{\mathbf{y}}_1(T + \eta) - \mathbf{y}_1(T + \eta)|}{|\mathbf{y}_1(T) - \mathbf{y}_1(T + \eta)|}. \quad (10)$$

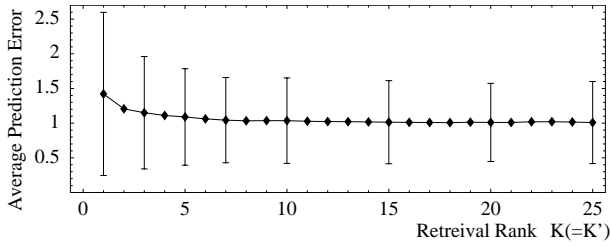


Figure 8: Average prediction error $\bar{\epsilon}_T$ in mesh feature space v.s. retrieval rank $K(=K')$, without thresholding by E_{TH} .

The prediction error ϵ_T in Eq.(10) was the distance between the actual future point and the predicted point at the lead time steps ahead, divided by persistence prediction error which is the distance between the query point and the actual future point, as shown in Figure 4. Normalization by the persistence prediction error was required to eliminate the dependency of the prediction error on the size of the individual echo pattern.

Figure 8 shows the transition of the average prediction error $\bar{\epsilon}_T$ and its standard deviation, as a function of the retrieval rank $K(=K')$, where no threshold E_{TH} is used. From Figure 8, we can see that the prediction error decreases as the rank $K(=K')$ increases and saturates at a certain level; the wide deviation range indicates that the prediction error varies widely depending on the sequences that neighbor each query. If the prediction error is above 1.0, the prediction is meaningless, because the prediction is worse than the persistence prediction that employs the query pattern as its forecast. In the case at $K(=K')=25$, 60.8% of all trials have prediction error under 1.0, and in such a case there is the potential to produce more accurate forecasts than would be possible with persistence prediction.

Evaluation of Forecast Images

Next, as a forecast image, we created the accumulated distribution of precipitation within periods from 2 hours to 3 hours later. The forecast images were calculated at five minute intervals from 2 hours to 3 hours later by Eq.(9), and each pixel value of the forecast images was transformed into precipitation intensity [mm/h] by applying a radar equation (Sauvageot 1992). Finally, the precipitation intensity at each time step was accumulated to yield the predicted distribution of the precipitation amount.

As a measure of forecast accuracy, we employed the CSI(Critical Success Index), which is the percentage of correctly forecasted areas divided by all areas including correctly forecasted areas and falsely forecasted areas whose precipitation exceeded 0.1[mm/hour]. Also, we employ the CSI ratio, which is a ratio of our result's CSI to the CSI of persistence forecasting. A persistence forecast is the accumulated distribution of precipitation from 1 hour before up to the query time. Generally speaking, overcoming the accuracy of persistence forecast is a primary goal of precipitation forecasting.

Table 1 shows the average CSI ratio and CSI for various $K(=K')$ values, where no threshold E_{TH} is used. From

Table 1: Average CSI ratio and average CSI for various retrieval rank $K(=K')$.

	$K=1$	$K=3$	$K=5$	$K=10$	$K=25$
CSI Ratio	0.76	0.97	1.02	1.08	1.12
CSI[%]	21.4	26.8	28.3	29.5	30.3

Table 2: Average CSI ratio and average CSI by simple extrapolation method (Rows of $K(=K')=3,10,25$ are results from same dataset for each MBF method).

	All	$K=3$	$K=10$	$K=25$
CSI Ratio	0.87	0.88	0.90	0.92
CSI[%]	18.8	19.1	18.6	17.2

Table 1, both CSI ratio and CSI are improved as $K(=K')$ increases, which corresponds to the trend in the prediction error as shown in Figure 8. At $K(=K')=25$, the CSI ratio reaches 1.12 and 51.8% of the forecasts exceeds the CSI of persistence forecasting. Table 2 shows the average CSI ratio and CSI by the simple extrapolation method for all samples and samples that correspond to our MBF method. The simple extrapolation method we use translates the present pattern at a single dominant velocity obtained by pattern matching between frames. A comparison of Table 1 and Table 2 shows that our MBF method exceeds the simple extrapolation method in terms of accuracy.

Figure 9 shows examples of forecast images, actual patterns, and persistence forecasts. Case 1) is the forecast created from the retrieval trial in Figure 7. We can see that thick line-shaped echo pattern changes into a widely spread pattern with a stripe-type texture over the sea within three hours. Case 2) and Case 3) are stratiform type pattern, which rapidly flows toward the upper-right direction with abrupt appearance of large surfaces. These cases confirm one key superiority of the MBF method: making the most of past patterns. The conventional methods fail to predict such drastic pattern changes, because they mainly depend on the current pattern.

Accordingly, our MBF framework is expected to become a promising tool to support the forecasting of local precipitation patterns by providing both retrieval and forecast images.

Discussion

In our framework, the forecast performance depends heavily on the dataset available. If there is no stored sequence that is similar to a given query sequence, the accuracy of retrieval and forecasting is greatly degraded; this is the main drawback of our MBF approach. Accordingly, it is useful to discover the relationship between the amount of stored data and forecast accuracy, and to know the degree of forecast reliability or predictability in advance. For guidance, we found a correlation between the retrieval error and the prediction error.

Furthermore, this work is rather simplistic in that only radar image information is used. Given that precipitation is affected by several physical atmospheric factors, the addi-

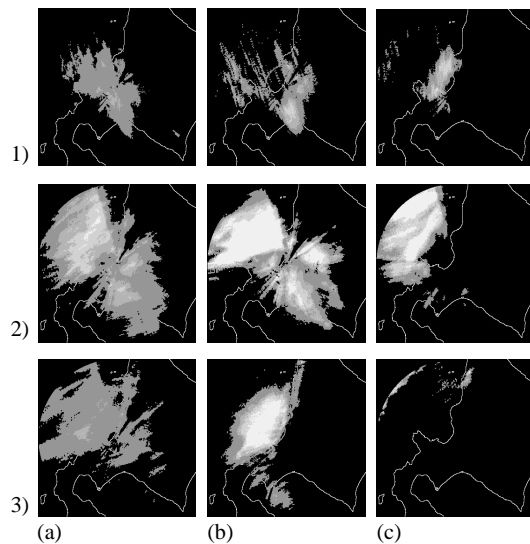


Figure 9: Accumulated distribution of precipitation from 2 hours later to 3 hours later, (a)Our forecast, (b)Actual, (c)Persistence forecast. For three cases, our CSI=(44.5, 72.9, 41.9), and CSI of persistence forecast is (16.5, 35.9, 3.0), respectively. No threshold E_{TH} is used, and $K=25$. Moreover, CSI of the simple extrapolation method was (24.2,24.0,1.0).

tion of physical information such as temperature, pressure, and humidity may be important in providing more accurate forecasts. For that purpose, appropriate selection and weighting mechanisms of different kinds of features should be incorporated into the MBF system.

Conclusion

This paper proposed a framework called Memory-Based Forecasting(MBF) and an implementation that can forecast complex natural patterns, especially weather radar echo patterns. To characterize such patterns, global features and temporal texture features were developed, and similar sequences are retrieved based on a dissimilarity measure between paths in the feature spaces. Several experiments confirmed that MBF offers good forecast accuracy if there is a sufficient volume and quality of stored data.

Acknowledgments. The authors are very grateful to Sapporo Information Network Co. and Mr. Masaharu Fujii for providing the radar images and useful meteorological advice. We also thank Dr. Noboru Sonehara of NTT Cyber Solutions Labs. for giving us the opportunity for this research.

References

- Bobick, A. F., and Wilson, A. D. 1995. A state-based technique for the summarization and recognition of gesture. In *Proc. ICCV'95*, 382–388.
- Connell, M. E., and Utgoff, P. E. 1987. Learning to control a dynamic physical system. In *Proc. AAAI'87*, 456–460.

- Crook, N. A., and Tuttle, J. D. 1997. Short-term forecasting of summer precipitation using echo extrapolation, storm characteristics and model output. In *Proc. 7th Conf. Aviation, Range and Aerospace Meteorology*, 274–278.
- Fujimoto, Y.; Iwasa, H.; Yokoya, N.; and Takemura, H. 1996. Retrieval of image sequences based on similarity of trajectories in eigenspaces. *Tech. Report of IEICE PRMU96-110:49–56*. (In Japanese).
- Hansen, B. K., and Riordan, D. 1998. Fuzzy case-based prediction of ceiling and visibility. In *Proc. 1st. Conf. Artificial Intelligence of the American Meteorological Society*, 118–123.
- Ikeguchi, T., and Aihara, K. 1995. Prediction of chaotic time series with noise. *IEICE Trans. Fundamentals E78-A(10):1291–1298*.
- Jones, E. K., and Roydhouse, A. 1995. Intelligent retrieval of archived meteorological data. *IEEE Expert* 50–57.
- Kolodner, J. L. 1991. Improving human decision making through case-based decision aiding. *AI Magazine* 52–68.
- Lee, R. W.; Barcia, R. M.; and Khator, S. K. 1995. Case-based reasoning for cash flow forecasting using fuzzy retrieval. In *Proc. 1st. Int. Conf. Case-Based Reasoning*, 510–519.
- Mohri, T.; Nakamura, M.; and Tanaka, H. 1993. Weather forecasting using memory-based reasoning. In *Proc. 2nd. Int. Workshop on PPAI*, 40–45.
- Mulhern, F. J., and Caprara, R. J. 1994. A nearest neighbor model for forecasting market response. *Int. J. Forecasting* 10:191–207.
- Murase, H., and Nayar, S. K. 1995. Visual learning and recognition of 3-d objects from appearance. *Int. J. Computer Vision* 14(1):5–24.
- Nayar, S. K.; Nene, S. A.; and Murase, H. 1996. Subspace methods for robot vision. *IEEE Trans. Robotics and Automation* 12(5):750–758.
- Otsuka, K.; Horikoshi, T.; Suzuki, S.; and Fujii, M. 1998. Feature extraction of temporal texture based on spatiotemporal motion trajectory. In *Proc. ICPR'98*, 1047–1051.
- Otsuka, K.; Horikoshi, T.; Suzuki, S.; and Kojima, H. 1999. Memory-based forecasting of complex natural patterns by retrieving similar image sequences. In *Proc. ICIAP'99*, 874–879.
- Otsuka, K.; Horikoshi, T.; Kojima, H.; and Suzuki, S. 2000. Image sequence retrieval for forecasting weather radar echo pattern. *IEICE Trans. Inf. and Syst.* E83-D. (Forthcoming).
- Sauvageot, H. 1992. *Radar meteorology*. Artech House, Inc.
- Stanfill, C., and Waltz, D. 1986. Toward memory-based reasoning. *Commun. ACM* 29(12):1213–1228.
- Turk, M. A., and Pentland, A. P. 1991. Face recognition using eigenfaces. In *Proc. CVPR'91*, 586–591.
- Yacooob, Y., and Black, M. J. 1999. Parameterized modeling and recognition of activities. *Computer Vision and Image Understanding* 73(2):232–247.